IET Electric Power Applications

ORIGINAL RESEARCH OPEN ACCESS

Model-Free Adaptive Super-Twisting Sliding Mode Speed Control Based on RBFNN Estimator for PMLSM Drive Systems

Qingfang Teng[1] | Xiaojian Wang[1] | Kai Xu[2]

[1]School of Automation and Electrical Engineering, Lanzhou Jiaotong University, Lanzhou, China | [2]School of Electrical and Data Engineering, University of Technology Sydney, Sydney, Australia

Correspondence: Kai Xu (Kai.Xu@student.uts.edu.au)

Received: 12 February 2025 | **Revised:** 24 April 2025 | **Accepted:** 5 May 2025

Handling Editor: Shuangxia Niu

Funding: The National Natural Science Foundation of China (No. 61463025, No. 62063015).

Keywords: adaptive super-twisting sliding mode control | permanent magnet linear synchronous motor | radial basis function neural network estimator | ultralocal model

ABSTRACT

Considering the various unknown and uncertain parameters as well as load disturbances of permanent magnet linear synchronous motor (PMLSM) drive systems, this paper proposes a novel model-free adaptive super-twisting (MFAST) speed control strategy based on radial basis function neural network (RBFNN) estimator to ensure the satisfactory performance and strong robustness of the speed control. First, by considering all possible unknown and uncertain parameters, the ultralocal model of PMLSM is constructed. Next, the RBFNN estimator is designed to estimate the unknown parameters of the above-mentioned ultralocal model. Finally, the RBFNN-based MFAST control law is proposed to guarantee PMLSM drive systems' robustness against various internal and external disturbances. StarSim HIL experiment results demonstrate that the synthesised RBFNN-based MFAST control strategy can enable PMLSM drive systems to possess high accuracy, remarkable rapidity and strong robustness.

1 | Introduction

At present, the permanent magnet linear synchronous motor (PMLSM) has been widely applied in many fields such as CNC machine tools, photolithography machines, rail transit equipment, logistics equipment, ropeless elevators, etc. [1], benefiting from its outstanding features of high thrust, high precision, high speed, high power density, rapid response and low noise. In addition, thanks to eliminating intermediate transmission links including ball screw and coupling, PMLSM could directly drive the load. Nevertheless, uncertain machine parameters, unknown nonlinear friction and thrust ripple and load variation inevitably exist, which cannot be ignored when designing control methods for PMLSM drive systems [2, 3]. Therefore, it is necessary to study feasible and effective control strategies to enhance the system's robustness and improve dynamic and steady-state performances against various uncertain and unknown factors for electrical machines [4].

For PMLSM drive systems, the PI control method is commonly used. However, it is highly sensitive to parameter mismatch and load disturbances, leading to poor dynamic performance. To improve system robustness against various internal and external disturbances, scholars have developed some advanced control methods such as adaptive control [5], active disturbance rejection control [6], model predictive control [7] as well as intelligent control [8, 9]. Apart from those methods, sliding mode control (SMC) [10] has been widely used due to its strong robustness, fast response and simple algorithm [11–13]. However, its discontinuous switching term results in chattering phenomena [14]. One effective solution to this problem is super-twisting control (STC), where the switching term is hidden in the integral [15, 16]. For conventional STC with constant gain, when subject to unknown or time-varying disturbances, it is challenging to select an appropriate gain to guarantee strong robustness, rapid dynamic response and weak chattering. Comparatively, the AST law with time-varying gain can adaptively adjust the control gain value to resist various unknown or time-varying disturbances, and thus make the system possess stronger robustness, faster response speed, better control accuracy and weaker chattering.

Despite its robust performance improvement, the model-based AST law cannot effectively control PMLSM drive systems with unknown and uncertain parameters. In response to such an issue, model-free AST (MFAST), based on an ultralocal model, which uses only the input and output of the system without considering any system parameters [17], can be proposed to solve the problem in this paper. As an essential part of the model-free control method, the observer estimates the ultralocal model's unknown parameters. At present, the commonly-used observers include Luenberger observer (LO), sliding mode observer (SMO), Kalman filter observer (KFO), extended state observer (ESO), etc. Ref. [18] employed LO to estimate the total disturbance of the PMSM such that deadbeat predictive current control is not affected by motor parameter mismatch, and internal and external interference. Ref. [19] constructed SMO to estimate the unknown parts of the novel model-free ultralocal model of PMSM to perform feedforward compensation. Ref. [20] used self-correction-based KFO for state estimation of the induction motor to ensure the accuracy and robustness of the prediction model. Using ESO, ref. [21] proposed model-free predictive current control of PMSM drives to achieve better performance in terms of current harmonics, tracking error and dynamic overshoot. Apart from the above-mentioned observers, new neural network observers have been emerging.

Given its fast approximation of any continuous function, the RBFNN-based observers have been brought into focus [22–24]. Currently, many researchers employ RBFNN-based observers to estimate ultralocal model parameters in different fields [25–28]. For this purpose, we construct an RBFNN-based observer to estimate unknown parameters of the ultralocal model of PMLSM, whose online training consists of the adaptive law for RBFNN weight matrices and an iterative algorithm for RBF centre values and widths.

In this study, we propose a novel RBFNN-based MFAST speed control strategy for PMLSM drive systems, which has rarely been reported. In the first place, the ultralocal model is built by taking into account various unknown and uncertain parameters and load disturbances. Then, using an RBFNN-based observer, the unknown parameters of the ultralocal model are estimated. Finally, the MFAST control law based on the RBFNN estimator is developed to obtain satisfactory speed control performance, and then its stability is analysed. Compared with the existing works, the main contributions of this paper are listed as follows:

1. The proposed strategy is essentially a model-free control method that does not require knowledge of motor parameters. It is a more practical engineering approach compared with the model-based control method.
2. As for the RBFNN estimator, its online training process is directly integrated into the MFAST control instead of the offline training process, which reduces operating costs.
3. The proposed RBFNN-based MFAST control strategy enhances the PMLSM drive system's robust performance under parameter variation and load disturbance.
4. In previous related literature, the stability analysis of the estimator and AST control law is usually independent; therefore, their stability is analysed separately. Although based on the state space model that integrates the RBFNN estimator with the AST controller, we prove the stability of the RBFNN-based MFAST. Compared with the separate analysis method, the systemic one in this study is more reasonable and more significant.

The remainder of this paper is organised as follows: in Section 2, based on the dynamic model of PMLSM, its ultralocal model is built. In Section 3, the RBFNN-based AST control law is designed, and its stability is analysed. In Section 4, the experimental verification results are presented; finally, conclusions are drawn in Section 5.

2 | Ultralocal Model of PMLSM Drive System

The dynamic model of the PMLSM drive system is expressed as follows:

$$M\frac{\mathrm{d}v_m}{\mathrm{d}t} = F_e - F_\Sigma - F_l - Bv_m, \quad F_e = n_p\frac{3\pi}{2\tau}\psi_f i_q \tag{1}$$

where F_e is the electromagnetic thrust; n_p is the number of pole pairs; τ is the magnetic flux per pole; ψ_f is the permanent magnet flux linkage, i_q is the q-axis stator current; M is the mover mass; v_m is the mover speed; F_Σ is the total disturbance force composed of unknown nonlinear friction and thrust ripple; F_l is the external load and B is the viscous friction coefficient.

Assume that the real values of M, ψ_f, B, F_Σ and F_l are unknown or uncertain, on the basis of Equation (1), the ultralocal model of the PMLSM can be built as follows:

$$\frac{\mathrm{d}v_m}{\mathrm{d}t} = gu + f \tag{2}$$

where u is the q-axis stator current; g and f are the unknown parameters whose expressions are given below:

$$g = \frac{3\pi n_p}{2\tau M}\psi_f, \quad f = -\frac{F_\Sigma + F_l}{M} - \frac{B}{M}v_m \tag{3}$$

3 | The RBFNN-Based MFAST Control Strategy

For the PMLSM drive system, the dual closed-loop control method with an outer speed loop and an inner current loop is adopted in this study. The current loop employs PI-based vector control, whereas the speed loop employs the proposed

RBFNN-based MFAST control strategy, which is the core design of this research study. The control block diagram of the PMLSM drive system is shown in Figure 1, whose control objective is to resist the adverse effects of parameter mismatches and load disturbances and thus ensure that the systems track the reference speed accurately and swiftly.

3.1 | RBFNN Estimator

The RBFNN estimator, shown in Figure 2, consists of three layers: an input layer, a hidden layer, and an output layer. By use of RBF, the input data is nonlinearly mapped to the hidden layer, and then by adjusting the RBF weights, the output layer can fit complex functional relationships [29].

In Figure 2, e_{v_m}, $\hat{f}$ and $\hat{g}$ are the inputs and outputs of the RBFNN estimator. e_{v_m} is defined as the speed error of the PMLSM, whereas $\hat{f}$ and $\hat{g}$ are the estimated values of f and g, respectively. They can be expressed as follows:

$$e_{v_m} = v_m - v_{m\mathrm{ref}} \tag{4}$$

$$\hat{f} = \mathbf{W}_f^{\mathrm{T}}\mathbf{H}_f + f_0, \quad \hat{g} = \mathbf{W}_g^{\mathrm{T}}\mathbf{H}_g + g_0 \tag{5}$$

where v_{mref} is the reference speed of the PMLSM; f_0 and g_0 are f and g that correspond to the nominal values of PMLSM; $\mathbf{W}_f$ and $\mathbf{W}_g$ are the RBF weight matrices; $\mathbf{H}_f$ and $\mathbf{H}_g$ are the hidden layer matrices. f_0, g_0, $\mathbf{W}_f$, $\mathbf{W}_g$, $\mathbf{H}_f$, and $\mathbf{H}_g$ are expressed as follows:

$$f_0 = -\frac{\text{Initial value of } F_l}{M_{\mathrm{nominal}}}, \quad g_0 = \frac{3\pi n_p}{2\tau_{\mathrm{nominal}} M_{\mathrm{nominal}}}\psi_{f\mathrm{nominal}} \tag{6}$$

$$\begin{aligned} \mathbf{W}_f &= [w_1\ w_2\ w_3\ w_4\ w_5]^{\mathrm{T}}, & \mathbf{W}_g &= [w_6\ w_7\ w_8\ w_9\ w_{10}]^{\mathrm{T}} \\ \mathbf{H}_f &= [h_1\ h_2\ h_3\ h_4\ h_5]^{\mathrm{T}}, & \mathbf{H}_g &= [h_6\ h_7\ h_8\ h_9\ h_{10}]^{\mathrm{T}} \end{aligned} \tag{7}$$

where M_{nominal}, τ_{nominal} and $\psi_{f\mathrm{nominal}}$ are the nominal value of M, τ and ψ_f.

In Equation (7), w_j (j = 1,2,...,10) is the weight of the jth hidden layer node; h_j (j = 1,2,...,10) is the radial basis functions, whose expressions is given as follows:

$$h_j = \exp\left(-\frac{(e_{v_m} - c_j)^2}{2b_j^2}\right) \tag{8}$$

In Equation (8), c_j and b_j are the RBF centre values and RBF widths of the jth hidden layer node, respectively.

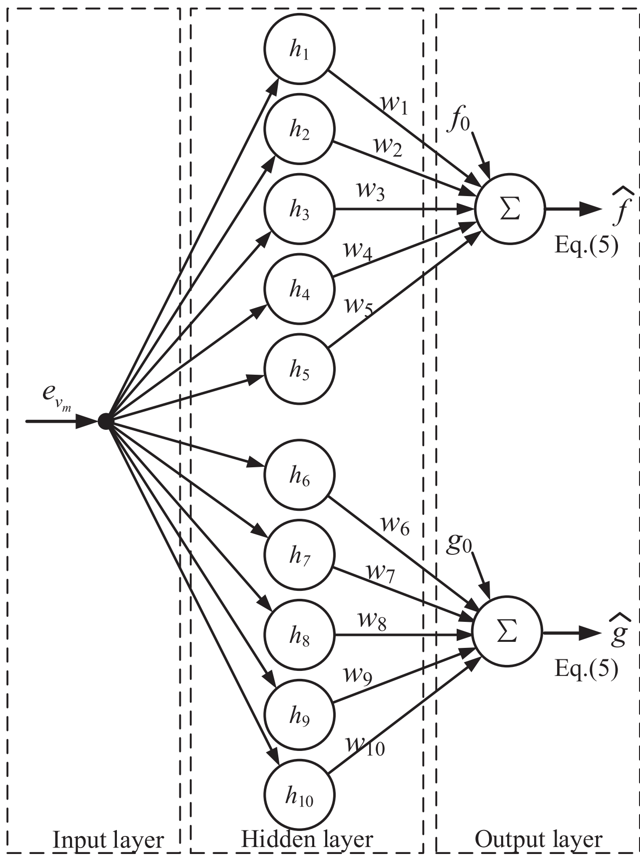

FIGURE 2 | RBFNN estimator.

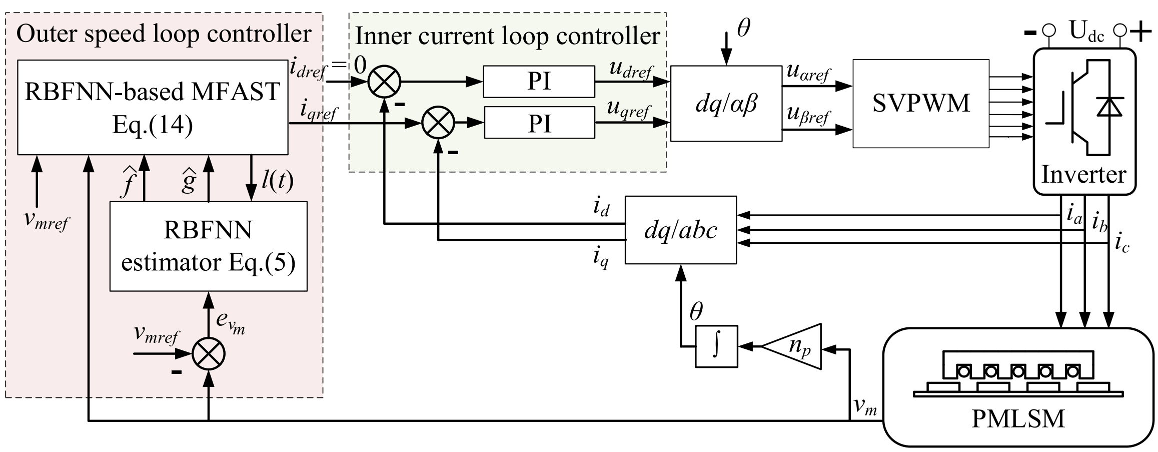

FIGURE 1 | Control block diagram of the PMLSM drive system.

3.1.1 | Adaptive Law for RBFNN Weight Matrices

The adaptive law for RBFNN weight matrices is designed as follows:

$$\begin{aligned}\frac{\mathrm{d}\mathbf{W}_f}{\mathrm{d}t} &= \left[3l^2(t)\mathrm{sign}\left(e_{v_m}\right) + \frac{\left|e_{v_m}\right|^{-1/2}l(t)}{2}\int l^2(t)\mathrm{sign}\left(e_{v_m}\right)\mathrm{d}t\right]\mathbf{H}_f \\ \frac{\mathrm{d}\mathbf{W}_g}{\mathrm{d}t} &= \left[3l^2(t)\mathrm{sign}\left(e_{v_m}\right) + \frac{\left|e_{v_m}\right|^{-1/2}l(t)}{2}\int l^2(t)\mathrm{sign}\left(e_{v_m}\right)\mathrm{d}t\right]u\mathbf{H}_g\end{aligned} \tag{9}$$

where $l(t)$ is the positive super-twisting sliding mode gain, which will be designed in Section 3.2.

The rationale for designing Equation (9) is based on the stability analysis of the RBFNN-based MFAST control law, which will be derived in Section 3.3.3.

3.1.2 | Iterative Algorithm for RBF Centre Values and Widths

In this paper, the K-means clustering method [30] is used to iteratively determine RBF centre values and widths in RBFNN. Consequently, at the $(k+1)$th sampling instant, the iterative algorithms for RBF centre values and RBF widths of the five hidden layer nodes used for estimating f as shown in Figure 2 are designed as follows:

$$\begin{cases} c_p(k+1) = c_p(k) + k_1\left[e_{v_m} - c_p(k)\right], & p = \underset{s.t.j=1,2,\cdots,5}{\arg\min}\left\{\left|e_{v_m} - c_j\right|\right\} \\ c_j(k+1) = c_j(k), & j = 1, 2, \cdots, 5, j \neq p \end{cases} \tag{10}$$

$$b_j = \frac{\max(c_j) - \min(c_j)}{\sqrt{6}}, j = 1, 2, \cdots, 5 \tag{11}$$

Similarly, at the $(k + 1)$ th sampling instant, the iterative algorithms for RBF centre values and RBF widths of the five hidden layer nodes used for estimating g as shown in Figure 2 are designed as follows:

$$\begin{cases} c_q(k+1) = c_q(k) + k_2\left[e_{v_m} - c_q(k)\right], & q = \underset{s.t.j=6,7,\cdots,10}{\arg\min}\left\{\left|e_{v_m} - c_j\right|\right\} \\ c_j(k+1) = c_j(k), & j = 6, 7, \cdots, 10, j \neq q \end{cases} \tag{12}$$

$$b_j = \frac{\max(c_j) - \min(c_j)}{\sqrt{6}}, j = 6, 7, \cdots, 10 \tag{13}$$

In Equations (10) and (12), k_1 and k_2 are positive real learning rates.

3.2 | RBFNN-Based MFAST Speed Control Strategy

The sliding variable s is selected as follows:

$$s = e_{v_m} \tag{14}$$

The RBFNN-based MFAST speed control law is designed as follows:

$$u = \frac{1}{\hat{g}}\left(-2l(t)|s|^{1/2}\mathrm{sign}(s) - \int \frac{l^2(t)}{2}\mathrm{sign}(s)\mathrm{d}t - \hat{f} + \dot{v}_{mref}\right) \tag{15}$$

The adaptive law of $l(t)$ in Equation (15) is designed as follows:

$$\dot{l}(t) = \begin{cases} \dfrac{-k\left|e_{v_m}\right|^{-1/2}\left|3l(t)^2\left|e_{v_m}\right|^{1/2}\mathrm{sign}\left(e_{v_m}\right) + l(t)\int \frac{l^2(t)}{2}\mathrm{sign}\left(e_{v_m}\right)\mathrm{d}t\right|}{6l\left|e_{v_m}\right| + 2|s|^{1/2}\mathrm{sign}\left(e_{v_m}\right)\int \frac{l^2(t)}{2}\mathrm{sign}\left(e_{v_m}\right)\mathrm{d}t + \left(l(t) - \bar{l}\right)}, & l(t) \geq \bar{l} \\ \bar{l}, & l(t) < \bar{l} \end{cases} \tag{16}$$

where k and $\bar{l}$ are positive real numbers.

The rationale for designing Equation (16) is based on the stability analysis of the RBFNN-based MFAST control law, which will be derived in Section 3.3.3.

Remark 1. Obviously, $l(t)$ is related to both RBFNN estimator and MFAST. Appropriately tune k and $\bar{l}$ in Equation (16) such that its adaptive law can simultaneously achieve two objectives: on the one hand, the RBFNN estimator tracks the real f and g accurately and rapidly; on the other, the MFAST control law improves the system's dynamic and steady-state performance while attenuating PMLSM system chattering. Consequently, the advantage of the adaptive law of $l(t)$ lies in that the stability of the PMLSM drive system and the convergence of the RBFNN estimator can be guaranteed simultaneously.

3.3 | Stability Analysis of the RBFNN-Based MFAST Control Strategy

To facilitate the stability analysis of the RBFNN-based MFAST control law, some variables related to the RBFNN are first defined. Then, the state-space model is established, which combines the RBFNN estimator with the AST control law. Finally, the stability of RBFNN-based MFAST is analysed based on the state-space model.

3.3.1 | Definitions of Some Variables for RBFNN Estimator

First, ε_f and ε_g are used to represent the RBFNN estimation errors as follows:

$$\begin{aligned}\varepsilon_f &= f - \hat{f} = f - \left(\mathbf{W}_f^{\mathrm{T}}\mathbf{H}_f + f_0\right) \\ \varepsilon_g &= g - \hat{g} = g - \left(\mathbf{W}_g^{\mathrm{T}}\mathbf{H}_g + g_0\right)\end{aligned} \tag{17}$$

Second, $\mathbf{W}_{fideal}$ and $\mathbf{W}_{gideal}$ are used to represent the RBF weight matrices that correspond to the minimum of the absolute estimation errors. Correspondingly, ε_{fideal} and ε_{gideal} denote the minimum of estimation errors as follows:

$$\begin{aligned}\varepsilon_{fideal} &= f - \left(\mathbf{W}_{fideal}^{\mathrm{T}}\mathbf{H}_f + f_0\right)\\ \varepsilon_{gideal} &= g - \left(\mathbf{W}_{gideal}^{\mathrm{T}}\mathbf{H}_g + g_0\right)\end{aligned} \tag{18}$$

and

$$\left|\varepsilon_{fideal}\right| = \min\left(\left|\varepsilon_f\right|\right), \left|\varepsilon_{gideal}\right| = \min\left(\left|\varepsilon_g\right|\right) \tag{19}$$

In Equation (18), $\mathbf{W}_{fideal}$ and $\mathbf{W}_{gideal}$ are given as follows:

$$\mathbf{W}_{fideal} = \left[w_1^* w_2^* w_3^* w_4^* w_5^*\right]^{\mathrm{T}}, \mathbf{W}_{gideal} = \left[w_6^* w_7^* w_8^* w_9^* w_{10}^*\right]^{\mathrm{T}} \tag{20}$$

where w_j^* (j = 1,2,...,10) is the weight of the jth hidden layer node of the RBFNN, which can minimise the absolute values of ε_f and ε_g.

Finally, $\Delta\mathbf{W}_f$ and $\Delta\mathbf{W}_g$ are used to represent the difference between $\mathbf{W}_f$ and $\mathbf{W}_{fideal}$ and the difference between $\mathbf{W}_g$ and $\mathbf{W}_{gideal}$ as follows:

$$\begin{aligned}\Delta\mathbf{W}_f &= \mathbf{W}_{fideal} - \mathbf{W}_f\\ \Delta\mathbf{W}_g &= \mathbf{W}_{gideal} - \mathbf{W}_g\end{aligned} \tag{21}$$

Consequently, the estimation error of the RBFNN estimator can be expressed as follows:

$$\begin{aligned}\varepsilon_f &= \left(\mathbf{W}_{fideal}^{\mathrm{T}}\mathbf{H}_f + f_0 + \varepsilon_{fideal}\right) - \left(\mathbf{W}_f^{\mathrm{T}}\mathbf{H}_f + f_0\right) = \Delta\mathbf{W}_f^T\mathbf{H}_f + \varepsilon_{fideal}\\ \varepsilon_g &= \left(\mathbf{W}_{gideal}^{\mathrm{T}}\mathbf{H}_g + g_0 + \varepsilon_{gideal}\right) - \left(\mathbf{W}_g^{\mathrm{T}}\mathbf{H}_g + g_0\right) = \Delta\mathbf{W}_g^{\mathrm{T}}\mathbf{H}_g + \varepsilon_{gideal}\end{aligned} \tag{22}$$

3.3.2 | The State-Space Model Combining RBFNN Estimator and AST Control Law

For the sake of conciseness, in what follows, l is used in place of $l(t)$ in Equations (15) and (16).

Define the state variables x_1, x_2 as follows:

$$x_1 = s, x_2 = -\int \frac{l^2}{2}\mathrm{sign}(s)\mathrm{d}t \tag{23}$$

Then, the second-order state equation combining the RBFNN estimator and AST control law can be presented as follows:

$$\begin{cases}\dot{x}_1 = \dot{s} = \dot{v}_m - \dot{v}_{mref} = gu + f - \dot{v}_{mref}\\ \dot{x}_2 = -\dfrac{l^2}{2}\mathrm{sign}(x_1)\end{cases} \tag{24}$$

In Equation (24), x_1 can be rewritten as follows:

$$\begin{aligned}\dot{x}_1 &= (g - \hat{g})u + \left(f - \hat{f}\right) + \hat{g}u + \hat{f} - \dot{v}_{mref}\\ &= \varepsilon_g u + \varepsilon_f + \hat{g}u + \hat{f} - \dot{v}_{mref}\end{aligned} \tag{25}$$

Considering Equations (15) and (25), Equation (24) is equivalent to the following equation:

$$\begin{cases}\dot{x}_1 = -2l|x_1|^{1/2}\mathrm{sign}(x_1) + x_2 + p\\ \dot{x}_2 = -\dfrac{l^2}{2}\mathrm{sign}(x_1)\end{cases} \tag{26}$$

where

$$p = \varepsilon_g u + \varepsilon_f \tag{27}$$

Substituting Equation (22) into Equation (27) yields the following equation:

$$p = \left(\Delta\mathbf{W}_g^T\mathbf{H}_g + \varepsilon_{gideal}\right)u + \Delta\mathbf{W}_f^T\mathbf{H}_f + \varepsilon_{fideal} \tag{28}$$

In fact, the stability analysis of the RBFNN-based MFAST is equivalent to that of the system of Equation (26).

3.3.3 | Stability Analysis of the RBFNN-Based MFAST Control Law

Inspired by ref. [31], a Lyapunov function is defined as follows:

$$V(x) = V_1(x) + V_2(x) + V_3(x) \tag{29}$$

where

$$\begin{aligned}V_1(x) &= \boldsymbol{\zeta}^{\mathrm{T}}\mathbf{P}\boldsymbol{\zeta}\\ V_2(x) &= \frac{1}{2}\Delta\mathbf{W}_f^{\mathrm{T}}\Delta\mathbf{W}_f + \frac{1}{2}\Delta\mathbf{W}_g^{\mathrm{T}}\Delta\mathbf{W}_g = \frac{1}{2}\sum_{j=1}^{10}\left(w_j^* - w_j\right)^2\\ V_3(x) &= \frac{1}{2}\left(l - \bar{l}\right)^2\end{aligned} \tag{30}$$

and

$$\boldsymbol{\zeta}^{\mathrm{T}} = [\zeta_1, \zeta_2] = [|x_1|^{1/2}\mathrm{sign}(x_1), x_2], \mathbf{P} = \begin{bmatrix}3l^2 & -l\\ -l & 1\end{bmatrix} \tag{31}$$

The derivative of $V_1(x)$ is given by the following equation:

$$\dot{V}_1(x) = 6l\dot{l}\zeta_1^2 + 6l^2\zeta_1\dot{\zeta}_1 - 2\dot{l}\zeta_1\zeta_2 - 2l\left(\dot{\zeta}_1\zeta_2 + \dot{\zeta}_2\zeta_1\right) + 2\zeta_2\dot{\zeta}_2 \tag{32}$$

Since,

$$\zeta_1 = \begin{cases}{x_1}^{1/2}, & x_1 \geq 0\\ -(-x_1)^{1/2}, & x_1 < 0\end{cases} \tag{33}$$

Thus,

$$\dot{\zeta}_1 = \begin{cases}\dfrac{1}{2}{x_1}^{-1/2}\dot{x}_1, & x_1 \geq 0\\ \dfrac{1}{2}(-x_1)^{-1/2}\dot{x}_1, & x_1 < 0\end{cases} \tag{34}$$

Furthermore,

$$\dot{\zeta}_1 = \frac{1}{2}|x_1|^{-1/2}\dot{x}_1 \tag{35}$$

Substituting $\dot{x}_1$ in Equation (26) and $[\zeta_1, \zeta_2]$ in Equation (31) into Equation (35) yields the following equation:

$$\begin{aligned}\dot{\zeta}_1 &= \frac{1}{2}|x_1|^{-1/2}\left(-2l|x_1|^{1/2}\mathrm{sign}(x_1) + x_2 + p\right)\\ &= \frac{1}{2}|x_1|^{-1/2}\left(-2l\zeta_1 + \zeta_2 + p\right)\end{aligned} \tag{36}$$

By considering $\zeta_2 = x_2$ in Equation (31) and $x_2 = -\int \frac{l^2}{2}\mathrm{sign}(s)dt$ in Equation (23) as well as $s = x_1$, the derivative of ζ_2 can be obtained as given bellow:

$$\begin{aligned}\dot{\zeta}_2 = \dot{x}_2 &= -\frac{l^2}{2}\mathrm{sign}(x_1) = -\frac{l^2}{2}\mathrm{sign}(x_1)|x_1|^{1/2}|x_1|^{-1/2}\\ &= -\frac{l^2}{2}|x_1|^{-1/2}\left(|x_1|^{1/2}\mathrm{sign}(x_1)\right)\end{aligned} \tag{37}$$

Substituting $\zeta_1 = |x_1|^{1/2}\mathrm{sign}(x_1)$ in Equation (31) into Equation (37) yields the following equation:

$$\dot{\zeta}_2 = -\frac{l^2}{2}|x_1|^{-1/2}\zeta_1 \tag{38}$$

By substituting Equations (36) and (38) into Equation (32), the derivative of $V_1(x)$ is given by the following equation:

$$\begin{aligned}\dot{V}_1(x) &= 3l^2\zeta_1(\zeta_2 - 2l\zeta_1 + p)|x_1|^{-1/2} - l^2\zeta_1\zeta_2|x_1|^{-1/2}\\ &\quad -2l\left[\frac{1}{2}\zeta_2(\zeta_2 - 2l\zeta_1 + p)|x_1|^{-1/2} - \frac{l^2}{2}\zeta_1^2|x_1|^{-1/2}\right] + b_1\\ &= -2l|x_1|^{-1/2}\left[\frac{5}{2}l^2\zeta_1^2 - 2l\zeta_1\zeta_2 + \frac{1}{2}\zeta_2^2\right] + b_2p + b_1\\ &= -|x_1|^{-1/2}\boldsymbol{\zeta}^{\mathrm{T}}\mathbf{Q}\boldsymbol{\zeta} + b_2p + b_1\end{aligned} \tag{39}$$

where,

$$\begin{aligned}&b_1 = 6l\dot{l}\zeta_1^2 - 2\dot{l}\zeta_1\zeta_2,\ b_2 = |x_1|^{-1/2}\left(3l^2\zeta_1 - l\zeta_2\right)\\ &\mathbf{Q} = l\begin{bmatrix}5l^2 & -2l\\ -2l & 1\end{bmatrix}\end{aligned} \tag{40}$$

At the same time, the derivatives of $V_2(x)$ and $V_3(x)$ are given as follows:

$$\begin{aligned}&\dot{V}_2(x) = -\sum_{j=1}^{10}\left(w_j^* - w_j\right)\dot{w}_j = -\Delta\mathbf{W}_f^{\mathrm{T}}\dot{\mathbf{W}}_f - \Delta\mathbf{W}_g^{\mathrm{T}}\dot{\mathbf{W}}_g\\ &\dot{V}_3(x) = \dot{l}\left(l - \bar{l}\right)\end{aligned} \tag{41}$$

Therefore, by combining Equation (39) with Equation (41), the derivative of $V(x)$ can be obtained as follows:

$$\begin{aligned}\dot{V}(x) &= \dot{V}_1(x) + \dot{V}_2(x) + \dot{V}_3(x)\\ &= -|x_1|^{-1/2}\boldsymbol{\zeta}^{\mathrm{T}}\mathbf{Q}\boldsymbol{\zeta} + b_2p + b_1 - \left(\Delta\mathbf{W}_f^{\mathrm{T}}\dot{\mathbf{W}}_f + \Delta\mathbf{W}_g^{\mathrm{T}}\dot{\mathbf{W}}_g\right)\\ &\quad + \dot{l}\left(l - \bar{l}\right)\end{aligned} \tag{42}$$

Substituting Equation (28) into Equation (42) yields follows:

$$\begin{aligned}\dot{V}(x) &= -|x_1|^{-1/2}\boldsymbol{\zeta}^{\mathrm{T}}\mathbf{Q}\boldsymbol{\zeta} + b_2\left[\left(\Delta\mathbf{W}_g^{\mathrm{T}}\mathbf{H}_g + \varepsilon_{gideal}\right)u\right.\\ &\quad \left.+\left(\Delta\mathbf{W}_f^{\mathrm{T}}\mathbf{H}_f + \varepsilon_{fideal}\right)\right] + b_1\\ &\quad -\left(\Delta\mathbf{W}_f^{\mathrm{T}}\dot{\mathbf{W}}_f + \Delta\mathbf{W}_g^{\mathrm{T}}\dot{\mathbf{W}}_g\right) + \dot{l}\left(l - \bar{l}\right)\\ &= -|x_1|^{-1/2}\boldsymbol{\zeta}^{\mathrm{T}}\mathbf{Q}\boldsymbol{\zeta} + \left(b_2\Delta\mathbf{W}_f^{\mathrm{T}}\mathbf{H}_f - \Delta\mathbf{W}_f^{\mathrm{T}}\dot{\mathbf{W}}_f\right)\\ &\quad + \left(b_2u\Delta\mathbf{W}_g^{\mathrm{T}}\mathbf{H}_g - \Delta\mathbf{W}_g^{\mathrm{T}}\dot{\mathbf{W}}_g\right)\\ &\quad - \left(\varepsilon_{gideal}u + \varepsilon_{fideal}\right)b_2 + b_1 + \dot{l}\left(l - \bar{l}\right)\end{aligned} \tag{43}$$

Inspired by [32], we let

$$b_2\Delta\mathbf{W}_f^{\mathrm{T}}\mathbf{H}_f - \Delta\mathbf{W}_f^{\mathrm{T}}\dot{\mathbf{W}}_f = 0 \quad b_2u\Delta\mathbf{W}_g^{\mathrm{T}}\mathbf{H}_g - \Delta\mathbf{W}_g^{\mathrm{T}}\dot{\mathbf{W}}_g = 0 \tag{44}$$

By taking Equation (44) into account, Equation (43) can be rewritten as follows:

$$\dot{V}(x) = -|x_1|^{-1/2}\boldsymbol{\zeta}^{\mathrm{T}}\mathbf{Q}\boldsymbol{\zeta} + \varepsilon b_2 + b_1 + \dot{l}\left(l - \bar{l}\right) \tag{45}$$

where,

$$\varepsilon = -\left(\varepsilon_{gideal}u + \varepsilon_{fideal}\right) \tag{46}$$

Substituting b_1 and b_2 into Equation (45) yields the following equation:

$$\begin{aligned}\dot{V}(x) &= -|x_1|^{-1/2}\boldsymbol{\zeta}^{\mathrm{T}}\mathbf{Q}\boldsymbol{\zeta} + \varepsilon|x_1|^{-1/2}\left(3l^2\zeta_1 - l\zeta_2\right) + 6l\dot{l}\zeta_1^2\\ &\quad - 2\dot{l}\zeta_1\zeta_2 + \dot{l}\left(l - \bar{l}\right)\end{aligned} \tag{47}$$

Let,

$$6l\dot{l}\zeta_1^2 - 2\dot{l}\zeta_1\zeta_2 + \dot{l}\left(l - \bar{l}\right) = -k|x_1|^{-1/2}\left|3l^2\zeta_1 - l\zeta_2\right| \tag{48}$$

Thereby, Equation (47) can be rewritten as follows:

$$\begin{aligned}\dot{V}(x) &= -|x_1|^{-1/2}\boldsymbol{\zeta}^{\mathrm{T}}\mathbf{Q}\boldsymbol{\zeta} + \varepsilon|x_1|^{-1/2}\left(3l^2\zeta_1 - l\zeta_2\right)\\ &\quad - k|x_1|^{-1/2}\left|3l^2\zeta_1 - l\zeta_2\right|\end{aligned} \tag{49}$$

Since

$$\lambda_{\min}(\mathbf{Q})\boldsymbol{\zeta}^{\mathrm{T}}\boldsymbol{\zeta} \le \boldsymbol{\zeta}^{\mathrm{T}}\mathbf{Q}\boldsymbol{\zeta} \le \lambda_{\max}(\mathbf{Q})\boldsymbol{\zeta}^{\mathrm{T}}\boldsymbol{\zeta} \tag{50}$$

where $\lambda_{\min}(\mathbf{Q})$ and $\lambda_{\max}(\mathbf{Q})$ are the minimum and maximum eigenvalues of $\mathbf{Q}$, respectively.

As a result, from Equation (49), we have the following inequality:

$$\begin{aligned}\dot{V}(x) &\le -|x_1|^{-1/2}\lambda_{\min}(\mathbf{Q})\boldsymbol{\zeta}^{\mathrm{T}}\boldsymbol{\zeta} + \varepsilon|x_1|^{-1/2}\left(3l^2\zeta_1 - l\zeta_2\right)\\ &\quad - k|x_1|^{-1/2}\left|3l^2\zeta_1 - l\zeta_2\right|\end{aligned} \tag{51}$$

Given that $\zeta_1 = |x_1|^{1/2}\mathrm{sign}(x_1)$ in Equation (31) is equivalent to $|\zeta_1| = |x_1|^{1/2}$, Equation (51) can be transformed into the following equation:

$$\dot{V}(x) \le -|\zeta_1|^{-1}\lambda_{\min}(\mathbf{Q})\boldsymbol{\zeta}^{\mathrm{T}}\boldsymbol{\zeta} + \varepsilon|\zeta_1|^{-1}(3l^2\zeta_1 - l\zeta_2) - k|\zeta_1|^{-1}|3l^2\zeta_1 - l\zeta_2| \tag{52}$$

Since,

$$\|\boldsymbol{\zeta}\| = \sqrt{\zeta_1^2 + \zeta_2^2} \ge |\zeta_1| \tag{53}$$

therefore,

$$\begin{aligned}\dot{V}(x) &\le -\|\boldsymbol{\zeta}\|^{-1}\lambda_{\min}(\mathbf{Q})\boldsymbol{\zeta}^{\mathrm{T}}\boldsymbol{\zeta} + \varepsilon|\zeta_1|^{-1}(3l^2\zeta_1 - l\zeta_2) - k|\zeta_1|^{-1}|3l^2\zeta_1 - l\zeta_2| \\ &= -\lambda_{\min}(\mathbf{Q})\|\boldsymbol{\zeta}\| + \varepsilon|\zeta_1|^{-1}(3l^2\zeta_1 - l\zeta_2) - k|\zeta_1|^{-1}|3l^2\zeta_1 - l\zeta_2| \\ &= \begin{cases} -\lambda_{\min}(\mathbf{Q})\|\boldsymbol{\zeta}\| + |\zeta_1|^{-1}(\varepsilon - k)(3l^2\zeta_1 - l\zeta_2), 3l^2\zeta_1 - l\zeta_2 \ge 0 \\ -\lambda_{\min}(\mathbf{Q})\|\boldsymbol{\zeta}\| + |\zeta_1|^{-1}(\varepsilon + k)(3l^2\zeta_1 - l\zeta_2), 3l^2\zeta_1 - l\zeta_2 < 0 \end{cases}\end{aligned} \tag{54}$$

Obviously, it can be seen from Equation (54) that regardless of whether $(3l^2\zeta_1 - l\zeta_2)$ is a positive or negative real number, as long as the inequality $k \ge |\varepsilon|$ holds, one can get the following equation:

$$\dot{V}(x) \le -\lambda_{\min}(\mathbf{Q})\|\boldsymbol{\zeta}\| \tag{55}$$

Matrix $\mathbf{Q}$ is positive definite whose analysis is given as follows:

As for $\mathbf{Q}$ in Equation (40), its two leading principal minors $\mathbf{D}_1$ and $\mathbf{D}_2$ are given by the following equations:

$$\mathbf{D}_1 = 5l^3, \mathbf{D}_2 = l \cdot (5l^2 - 4l^2) = l^3 \tag{56}$$

If $l > 0$, then $\mathbf{D}_1 > 0$ and $\mathbf{D}_2 > 0$ holds. On the other hand, if $l \le 0$, it can be seen from Equation (16) that $\dot{l}(t) = \bar{l} > 0$ holds, which implies that l monotonically increases until $l > 0$, thus $\mathbf{D}_1 > 0$ and $\mathbf{D}_2 > 0$ holds. In line with Sylvester theorem, $\mathbf{Q}$ is a positive definite matrix, and then $\lambda_{\min}(\mathbf{Q}) > 0$ holds. Consequently $\dot{V}(x) \le 0$ holds. According to Lyapunov theory, the system of Equation (26) is stable, that is , the RBFNN-based MFAST control strategy can guarantee the stability of the PMLSM drive systems.

Remark 2. There must exist k such that inequality $k \ge |\varepsilon|$ holds whose reason lies in that ε_{fideal} and ε_{gideal} as the minimums of estimation errors are very small real numbers, and u is a finite value. Accordingly, $|\varepsilon| = |\varepsilon_{gideal}u + \varepsilon_{fideal}|$ is a small positive real number. Apparently, k is selected such that $k \ge |\varepsilon|$ holds.

Remark 3. The design of the adaptive law of RBFNN weight matrices is as follows.

Because Equation (44) can be rewritten as follows:

$$\frac{\mathrm{d}\mathbf{W}_f}{\mathrm{d}t} = b_2\mathbf{H}_f, \quad \frac{\mathrm{d}\mathbf{W}_g}{\mathrm{d}t} = b_2 u\mathbf{H}_g \tag{57}$$

Substituting Equation (40) into Equation (57) yields the following equation:

$$\frac{\mathrm{d}\mathbf{W}_f}{\mathrm{d}t} = |x_1|^{-1/2}(3l^2\zeta_1 - l\zeta_2)\mathbf{H}_f, \quad \frac{\mathrm{d}\mathbf{W}_g}{\mathrm{d}t} = u|x_1|^{-1/2}(3l^2\zeta_1 - l\zeta_2)\mathbf{H}_g \tag{58}$$

Further, by considering Equations (31), Equation (58) can be rewritten as follows:

$$\begin{aligned}\frac{\mathrm{d}\mathbf{W}_f}{\mathrm{d}t} &= |x_1|^{-1/2}(3l^2|x_1|^{1/2}\mathrm{sign}(x_1) - lx_2)\mathbf{H}_f, \\ \frac{\mathrm{d}\mathbf{W}_g}{\mathrm{d}t} &= u|x_1|^{-1/2}(3l^2|x_1|^{1/2}\mathrm{sign}(x_1) - lx_2)\mathbf{H}_g\end{aligned} \tag{59}$$

Substituting Equation (23) into Equation (59) and considering $s = e_{v_m}$, we obtains the adaptive law for RBFNN weight matrices given in Equation (9).

Remark 4. The design of the adaptive law of l is as follows. Equation (48) can be written as follows.

$$\dot{l} = \frac{-k|x_1|^{-1/2}|3l^2\zeta_1 - l\zeta_2|}{6l\zeta_1^2 - 2\zeta_1\zeta_2 + (l - \bar{l})} \tag{60}$$

Substituting Equation (31) into Equation (60) yields the following equation:

$$\dot{l} = \frac{-k|x_1|^{-1/2}|3l^2|x_1|^{1/2}\mathrm{sign}(x_1) - lx_2|}{6l|x_1| - 2|x_1|^{1/2}\mathrm{sign}(x_1)x_2 + (l - \bar{l})} \tag{61}$$

Moreover, by Substituting Equation (23) into Equation (61) and then considering $s = e_{v_m}$, we can obtain the following equation:

$$\dot{l}(t) = \frac{-k|e_{v_m}|^{-1/2}\left|3l(t)^2|e_{v_m}|^{1/2}\mathrm{sign}(e_{v_m}) + l(t)\int\frac{l^2(t)}{2}\mathrm{sign}(e_{v_m})\mathrm{d}t\right|}{6l|e_{v_m}| + 2|s|^{1/2}\mathrm{sign}(e_{v_m})\int\frac{l^2(t)}{2}\mathrm{sign}(e_{v_m})\mathrm{d}t + (l(t) - \bar{l})} \tag{62}$$

To guarantee the positive definiteness of $\mathbf{Q}$ and thus the negative definiteness of $\dot{V}(x)$, we can obtain the final adaptive law of l given in Equation (16).

4 | Hardware-in-the-Loop Experimental Analysis

To verify the effectiveness and superiority of the proposed strategy, three PMLSM drive systems, named System 1, System 2, and System 3, were built in the StarSim HIL experimental platform shown in Figure 3, which consists of a real-time mode simulator, StarSim software, DSP(TMS320 F28335PGF), I/O board, a host computer and an oscilloscope. The speed control laws for those three systems were RBFNN-based MFAST, conventional STC and AST, respectively. Three systems employed the identical PI-based vector for inner current loop control. The nominal parameters of PMLSM and control parameters are listed in Table 1. The sampling period of the controller was 100us. F_{Σ} in Equation (1) was set as $5\sin 500t$.

4.1 | Comparison of the Control Effects Between System 1 and System 2

To verify its faster response, higher tracking accuracy and stronger robustness, System 1 was compared with System 2

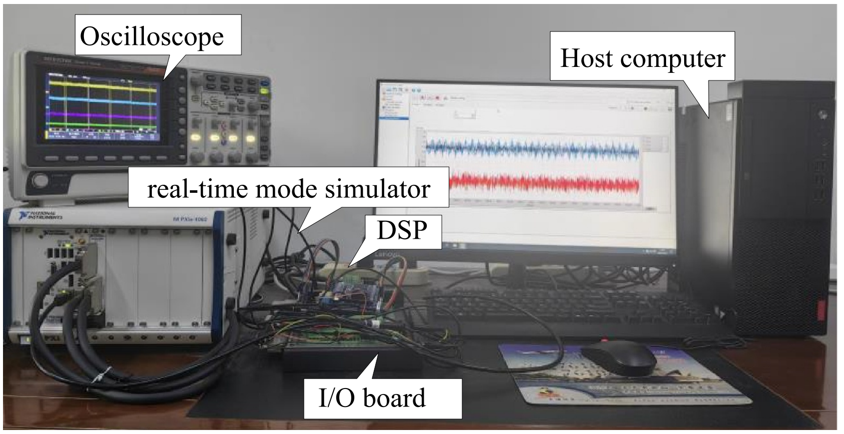

FIGURE 3 | StarSim HIL experimental platform.

TABLE 1 | Nominal parameters of PMLSMs and control parameters.

PMLSM parameters	Value	Control parameters	Value
U_{dc} (inverter DC bus voltage)	500 V	k_1, k_2	0.05, 0.02
R_s (stator resistance)	2.6 Ω	g_0, f_0	9, −15
L_s (inductance)	26.7 mH	$c_1(0) \sim c_{10}(0)$	3, 1, 0, −1, −3, 0.2, 0.1, 0, −0.1, −0.2
M	6.6 kg	$b_1(0) \sim b_{10}(0)$	10
ψ_f	0.24 Wb	k, $\bar{l}$	0.5, 20
τ, n_p	18 mm, 1	k_p and k_i (PI control gains of inner current loop)	80, 100
B	0.2 N·s/m	l_{stc1},l_{stc2}	1, 2

under three different operating conditions. The STC law of System 2 is designed as follows:

$$u = \frac{1}{g_0}\left(- l_{\text{stc1}}|s|^{1/2}\text{sign}(s) - \int l_{\text{stc2}}\text{sign}(s)\text{d}t - f_0 + \dot{v}_{mref} \right) \quad (63)$$

where l_{stc1} and l_{stc2} are the constant gains with values of 8.3 and 2.5, respectively. g_0 and f_0 are calculated by Equation (3) when the motor parameters are the nominal values given in Table 1.

4.1.1 | Comparison of System 1 and System 2 Under the Reference Speed Change

Figure 4b and 4c show the response waveforms of v_m, F_e, i_d, and i_q in System 1 and System 2, respectively, when the load F_l is 100 N and the given reference speed v_{mref} is a trapezoidal wave shown in Figure 4a.

Figure 4b shows that although v_m of both System 1 and System 2 could track v_{mref} before and after v_{mref} suddenly rises from −1 to 1 m/s, or suddenly drops from 1 to −1 m/s, the speed response of System 1 has no overshoot, whereas that of System 2 has an overshoot of 1 m/s/div × 0.6div = 0.6 m/s. In addition, the ripples of v_m and F_e of System 1 are significantly smaller than that of System 2 (in steady state, the ripples of v_m and F_e in System 1 are 1 m/s/div × 0.08div = 0.08 m/s and 100 N/div × 0.3div = 30 N, respectively, whereas in System 2, they are 1 m/s/div × 0.15div = 0.15 m/s and 100 N/div × 0.4div = 40 N, respectively). Figure 4c shows that the ripples of i_d and i_q in System 1 are 1 A/div × 0.3div = 0.3 and 1 A/div × 0.4div = 0.4 A, respectively, whereas in System 2, they are 1 A/div × 0.4div = 0.4 and 1 A/div × 0.6div = 0.6 A, respectively.

Those results indicate that compared to System 2, System 1 has a better dynamic and steady-state performance under reference speed change.

4.1.2 | Comparison of System 1 and System 2 Under Load Change

Figure 5b and 5c show the response of v_m, F_e, i_d and i_q in System 1 and System 2, respectively, when the given v_{mref} is 1 m/s and the given F_l is a rectangular wave shown in Figure 5a.

Figure 5b shows that although the speeds of two systems can track the reference before and after F_l suddenly drops from 100 to 50 N or suddenly rises from 50 to 100 N, the ripples of v_m and F_e of System 1 are significantly smaller than that of System 2 (in steady state, the ripples of v_m and F_e in system 1 are approximately 1 m/s/div × 0.08div = 0.08 m/s and 100 N/div × 0.3div = 30 N, respectively, whereas for System 2, they are approximately 1 m/s/div × 0.15div = 0.15 m/s and 100 N/div × 0.4div = 40 N, respectively). Figure 5c shows that the ripples of i_d and i_q of System 1 are approximately 1 A/div × 0.3div = 0.3 A, whereas for System 2, they are

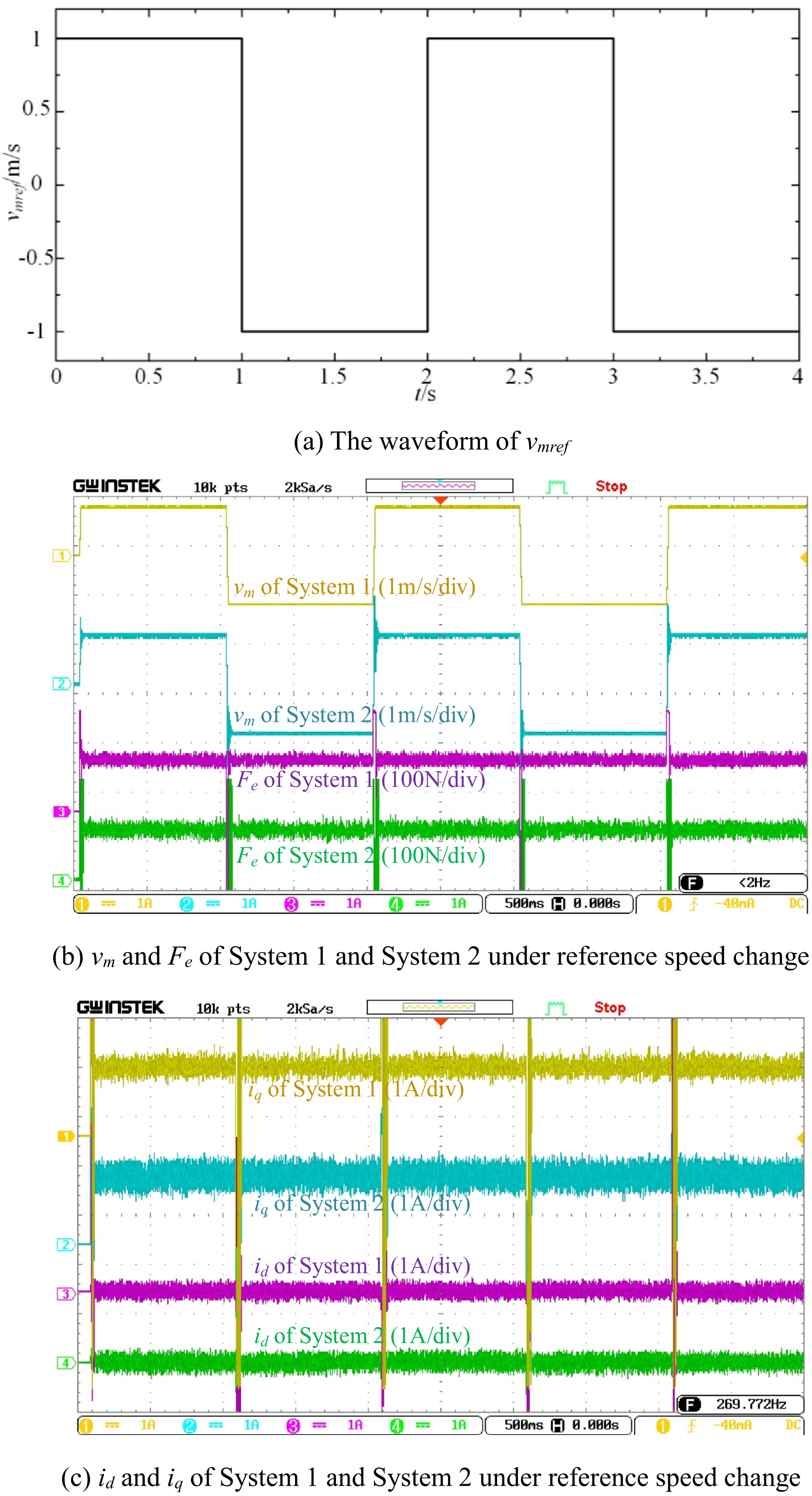

(a) The waveform of v_{mref}

(b) v_m and F_e of System 1 and System 2 under reference speed change

(c) i_d and i_q of System 1 and System 2 under reference speed change

FIGURE 4 | Comparison of System 1 and System 2 under reference speed change.

approximately 1 A/div × 0.4div = 0.4 A, which means that the ripples of i_d and i_q of System 1 are smaller than those of System 2.

Those results demonstrate that because of the smaller ripples of System 1 than those of System 2, the steady-state performance of System 1 is better than that of System 2 under load change.

4.1.3 | Comparison of System 1 and System 2 Under Permanent Magnet Flux Linkage Change

Figure 6b and 6c show the response waveforms of v_m, F_e, i_d and i_q in System 1 and System 2, respectively, when permanent magnet flux linkage ψ_f is increased from 0.24 to 0.36 Wb at 1 s as shown in Figure 6a, and load F_l is 100 N and the given v_{mref} is 1 m/s.

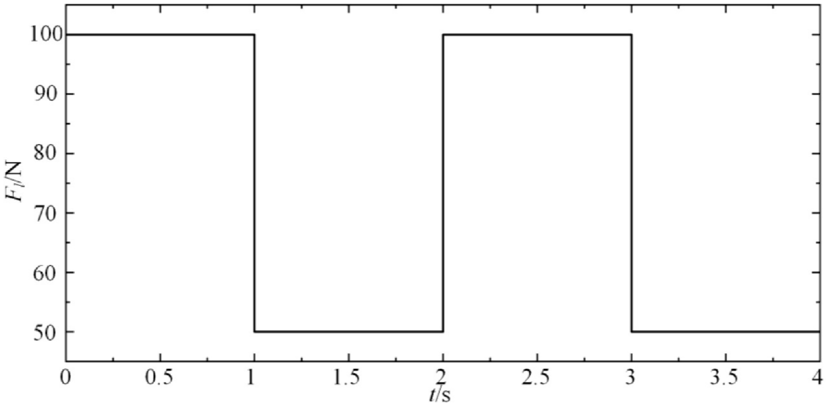

(a) The given waveform of F_l

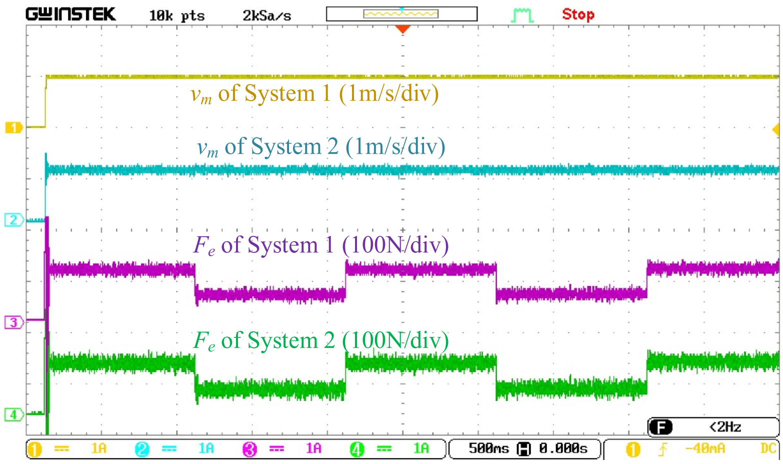

(b) v_m and Fe of System 1 and System 2 under load change

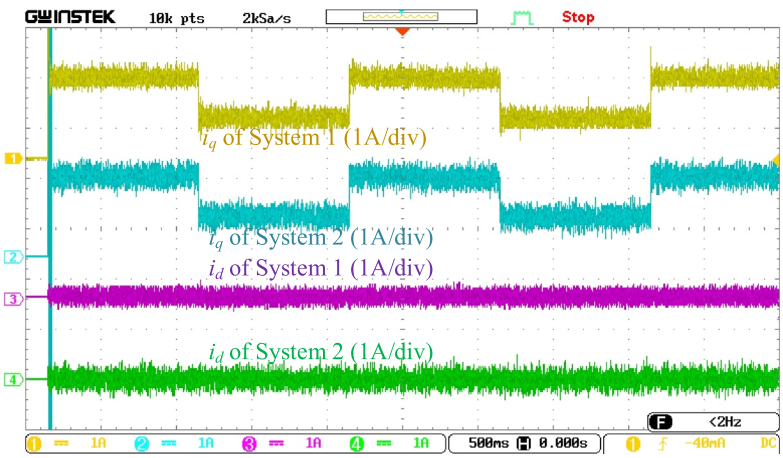

(c) i_d and i_q of System 1 and System 2 under load change

FIGURE 5 | Comparison of System 1 and System 2 under load change.

Figure 6b shows that before and after permanent magnet flux linkage ψ_f suddenly rises from 0.24 to 0.36 Wb at 1 s, the speeds of two systems could track the reference and the ripples of v_m and F_e in System 1 are approximately 1 m/s/div × 0.05div = 0.05 m/s and 100 N/div × 0.3div = 30 N, respectively, compared to approximately 1 m/s/div × 0.15div = 0.15 m/s and 100 N/div × 0.4div = 40 N of that in System 2. Figure 6c shows that before the step change of ψ_f, the ripples of i_d and i_q in System 1 are approximately 1 A/div × 0.3div = 0.3 A, compared to approximately 1 A/div × 0.4div = 0.4 A of that in System 2. After the step change of ψ_f, there is a step descent of i_q in two systems. The ripples of i_q in System 1 are approximately 1 A/div × 0.3div = 0.3 A, compared to approximately 1 A/div × 0.4div = 0.4 A of that in System 2. The ripple of i_d in System 1 remains unchanged, whereas the ripple of i_d in System 2 increases to 1 A/div × 1.2div = 1.2 A.

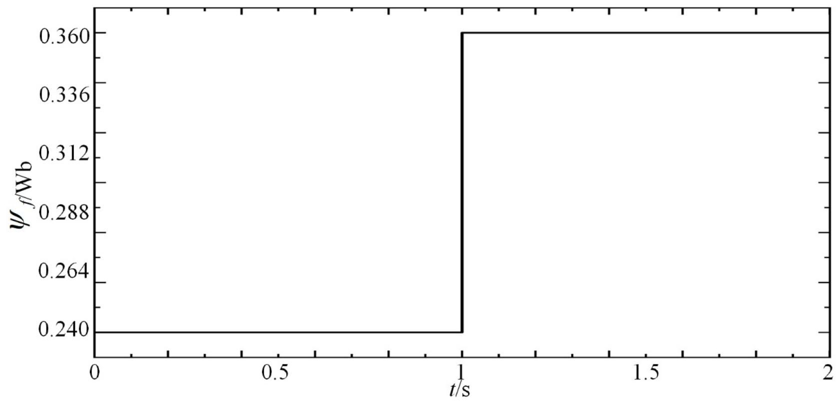

(a) The given waveform of ψ_f

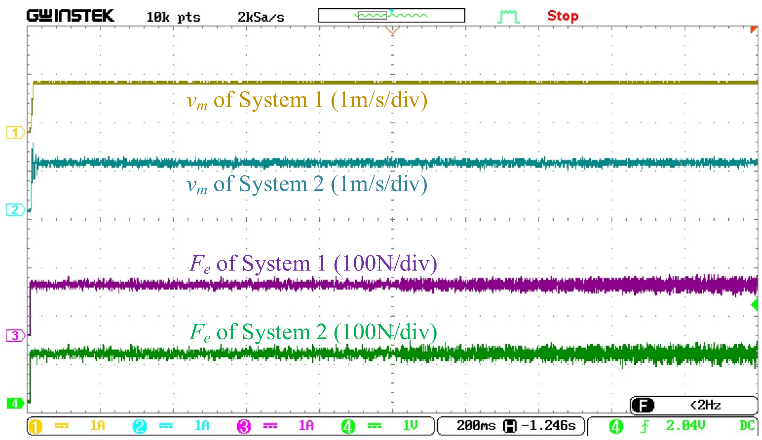

(b) v_m and Fe of System 1 and System 2 under ψ_f change

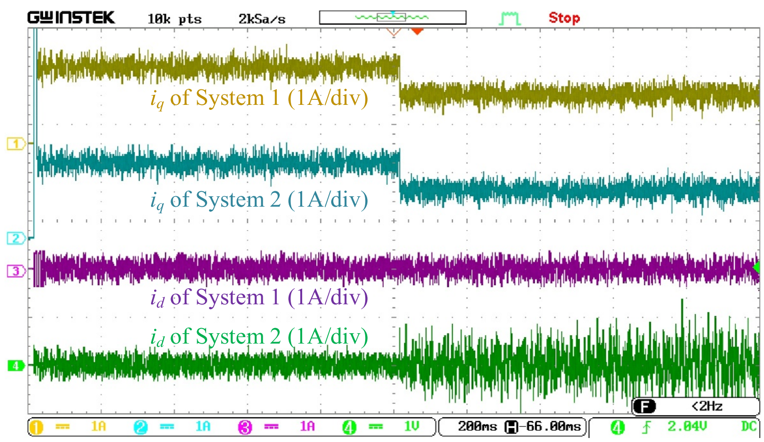

(c) i_d and i_q of System 1 and System 2 under ψ_f change

FIGURE 6 | Comparison of System 1 and System 2 under ψ_f change.

These results indicate that the ripples of System 1 are smaller than those of System 2 under ψ_f change.

By summing up the above-mentioned experiments of the three operation conditions, Table 2 presents the specification comparison between System 1 and System 2. It could be seen from Table 2 that compared with the conventional STC, the RBFNN-based MFAST control strategy has stronger robustness against reference speed change, load variation and permanent magnet flux linkage change, which is attributed to the collaborative action of the real-time RBFNN estimator and the AST with adaptive gain.

4.2 | Comparison of the Control Effects Between System 1 and System 3

To verify the accuracy and effectiveness of the designed RBFNN estimator in System 1, it is compared with System 3 under three

TABLE 2 | Specification comparison between System 1 and System 2.

Operation conditions	System	Ripple of v_m (m/s)	Overshoot of v_m (m/s)	Ripple of F_e (N)	Ripple of i_d (A)	Ripple of i_q (A)
v_{mref} change	System1	0.08	0	30	0.3	0.4
	System2	0.15	0.6	40	0.4	0.6
F_l change	System1	0.08	0	30	0.3	0.3
	System2	0.15	0.35	40	0.4	0.4
ψ_f change	System1	0.05	0	30	0.3 before ψ_f change	0.3 before ψ_f change
					0.3 after ψ_f change	0.3 after ψ_f change
	System2	0.15	0.35	40	0.4 before ψ_f change	0.4 before ψ_f change
					1.2 after ψ_f change	0.4 after ψ_f change

different operating conditions. The AST law of System 3 is designed as follows:

$$u = \frac{1}{g}\left(-2l(t)|s|^{1/2}\text{sign}(s) - \int \frac{l^2(t)}{2}\text{sign}(s)\text{d}t - f + \dot{v}_{mref} \right) \quad (64)$$

where g and f are calculated by Equation (3)

4.2.1 | Comparison of System 1 and System 3 Under the Reference Speed Change

When the load F_l is 100 N and the given reference speed v_{mref} is a trapezoidal wave shown in Figures 4a, 7a and b show the response waveforms of v_m, F_e, i_d, and i_q for System 1 and System 3, respectively. Figure 7c shows the waveforms of $\hat{f}$, $\hat{g}$ in System 1 and f, g in System 3. Figure 7d shows the waveforms of e_{v_m} and l in System 1.

Figure 7a shows that regardless of whether v_{mref} sharply rises from −1 to 1 m/s or drops from 1 to −1 m/s, the waveforms of v_m of System 1 and System 3 are almost identical, so are the waveforms of F_e. Similarly, it can be observed from Figure 7b that the waveforms of dq-axis currents of System 1 and System 3 are almost identical.

Figure 7c shows that regardless of whether v_{mref} sharply rises from −1 m/s to 1 m/s or drops from 1 m/s to −1 m/s, $\hat{f}$ and f are almost identical, so are $\hat{g}$ and g, which indicates $\hat{f}$ and $\hat{g}$ could track their true values f and g, respectively. Figure 7d shows that the speed error e_{v_m} almost remains zero, except that there are relatively large e_{v_m} at the step change instant of the reference speed, and meanwhile shows that l fluctuates around $\bar{l}$, which indicates that l could be adaptively adjusted with the change of e_{v_m} in order to track the given reference speed.

Those results indicate that the designed RBFNN estimator is feasible and effective, which guarantees that the RBFNN-based MFAST control strategy makes the PMLSM drive system track the given speed.

4.2.2 | Comparison of System 1 and System 3 Under Load Change

When v_{mref} is set as 1 m/s and F_l is set as a rectangular wave shown in Figures 5a, 8a and b show the response waveforms of v_m, F_e, i_d, and i_q for System 1 and System 3, respectively. Figure 8c shows the waveforms of $\hat{f}$, $\hat{g}$ in System 1 and f, g in System 3. Figure 8d shows the waveforms of e_{v_m} and l of System 1.

Figure 8a shows that the waveforms of v_m of System 1 and System 3 are almost the same, and so are the waveforms of F_e. Meanwhile, it can be seen from Figure 8b that the waveforms of dq-axis currents of System 1 and System 3 are almost the same.

Figure 8c shows that before and after F_l suddenly drops from 100 to 50 N or before and after suddenly rises from 50 to 100 N, $\hat{f}$ and f are almost identical, so are $\hat{g}$ and g, which indicates $\hat{f}$ and $\hat{g}$ could track their true values f and g, respectively. Figure 8d shows that the speed error e_{v_m} almost remains zero, and l fluctuates around $\bar{l}$, which indicates that l could be adaptively adjusted with the change of e_{v_m} in order to track the given reference speed.

Those results indicate that the designed RBFNN estimator is feasible and effective, and consequently, the RBFNN-based MFAST control strategy can be immune to load variation.

4.2.3 | Comparison of System 1 and System 3 Under the Step Change of Permanent Magnet Flux Linkage

When ψ_f is increased from 0.24 to 0.36 Wb at 1 s as shown in Figure 6a, and v_{mref} is set as 1 m/s and F_l is set as 100 N. Figure 9a and 9b show the response waveforms of v_m, F_e, i_d, and i_q for System 1 and System 3, respectively, and Figure 9c shows the waveforms of $\hat{f}$, $\hat{g}$ in System 1 and f, g in System 3. Figure 9d shows the waveforms of e_{v_m} and l of System 1.

Figure 9a shows that before and after step change of ψ_f, the waveforms of v_m of System 1 and System 3 remain unchanged

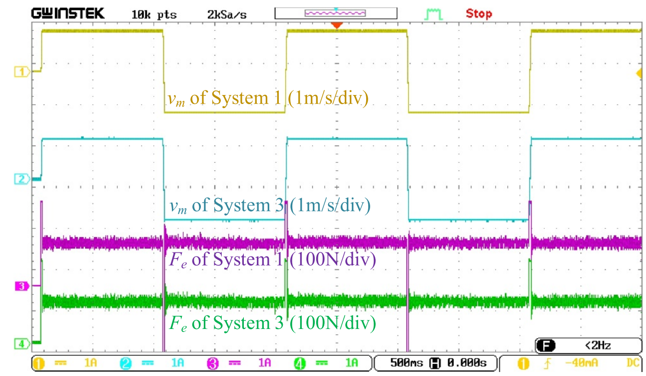

(a) v_m and F_e of System 1 and System 3 under reference speed change

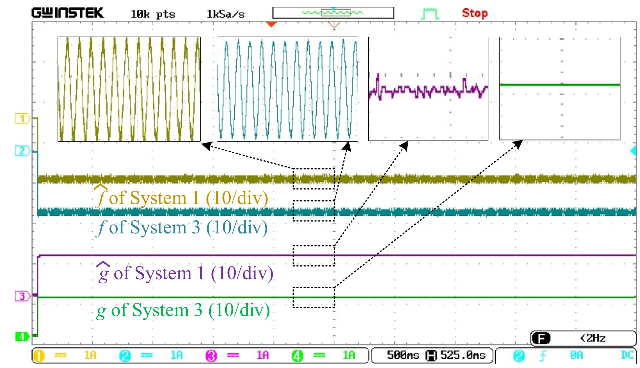

(c) $\hat{f}$, $\hat{g}$ of System 1 and f, g of System 3 under reference speed change

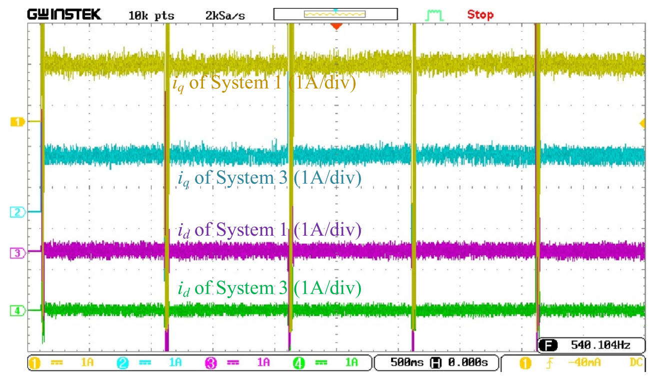

(b) i_d and i_q of System 1 and System 3 under reference speed change

(d) e_{v_m} and l of System 1 under reference speed change

FIGURE 7 | Comparison of System 1 and System 3 under reference speed change.

and are almost the same, whereas their ripples of F_e after ψ_f change are slightly larger than those before ψ_f change, but their ripples of F_e are almost the same.

Figure 9b shows that after ψ_f change, there is a step descent of i_q in two systems, but their waveforms of i_d remain unchanged. And the ripples of dq-axis currents of System 1 are slightly larger than those of System 3.

Figure 9c shows that before and after the step change of ψ_f, $\hat{f}$ and f remain unchanged and are almost identical. Meanwhile, after ψ_f change, there is an increase of $\hat{g}$ and g in two systems, but their waveforms are almost identical. Those results indicate that $\hat{f}$ and $\hat{g}$ could track their true values f and g, respectively under ψ_f change.

Figure 9d shows that the speed error e_{v_m} almost remains zero. It shows that l fluctuates around $\bar{l}$, which indicates that l could be adaptively adjusted with the change of e_{v_m} in order to track the given reference speed.

By summing up the above-mentioned experiments of the three operation conditions, Table 3 presents the specification comparison between System 1 and System 3. It could be seen from Table 3 that their ripples are slightly different, resulting from the estimation error of the RBFNN estimator. However, the designed RBFNN estimator is feasible and effective. Thus, the RBFNN-based MFAST control strategy has strong robustness against reference speed change, load variation, and permanent magnet flux linkage change.

Summarising these HIL experiments, we can obtain the following analysis results:

1. By comparing control effects between System 1 and System 3, the online RBFNN estimator is verified to be feasible and effective.
2. Without knowledge of any motor parameters, the model-free MFAST strategy is suitable for engineering applications.
3. Compared with conventional STC law, the RBFNN-based MFAST control strategy can not only enhance robustness against load disturbance but also significantly reduce system ripples and improve steady-state performance.

5 | Conclusion

In view of unknown and uncertain parameters as well as load disturbances, a powerful RBFNN-based MFAST control strategy was proposed to achieve high precision and strong robustness of the speed control for PMLSM drive systems. First, as for all unknown or uncertain parameters and load disturbance, based on the dynamic model of PMLSM, its ultralocal model was

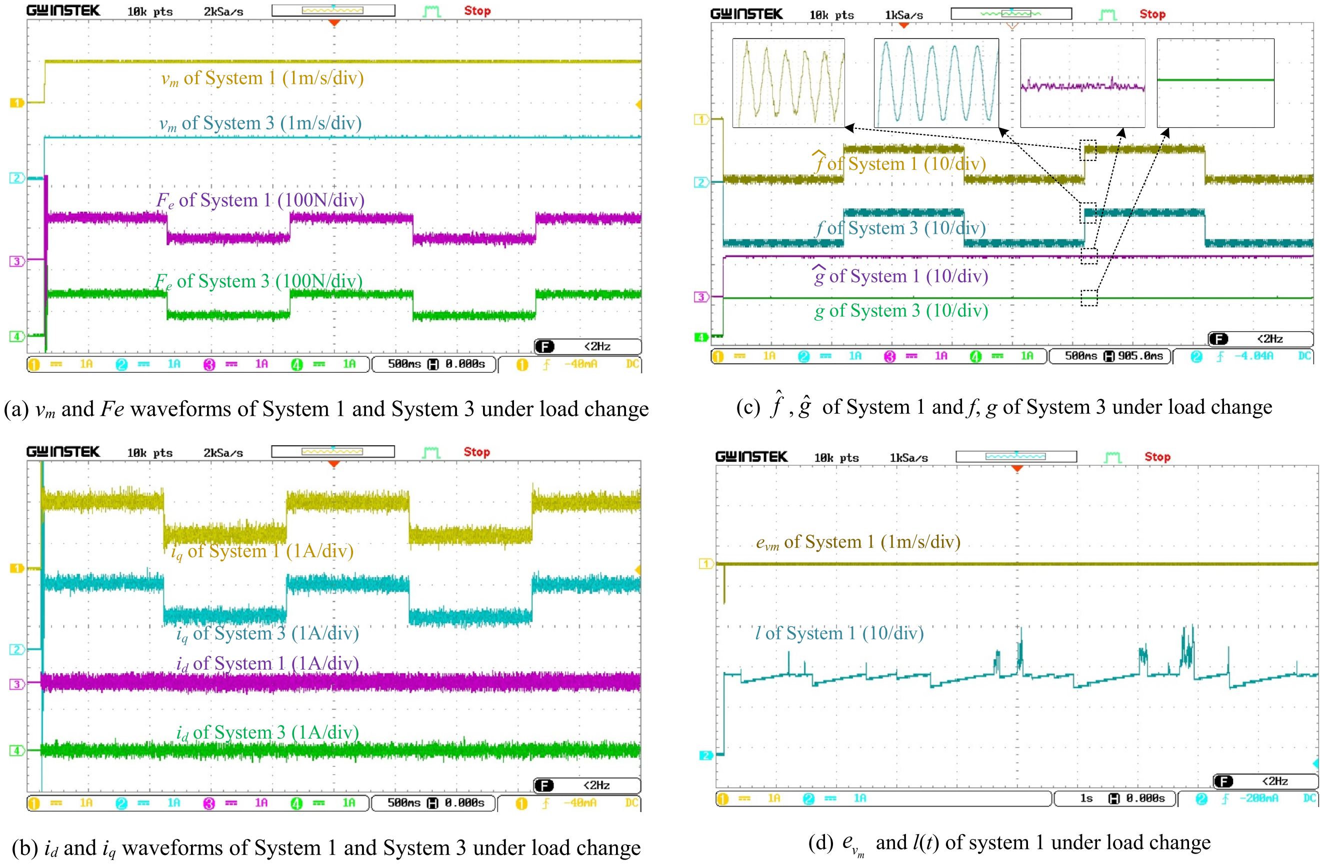

(a) v_m and Fe waveforms of System 1 and System 3 under load change

(c) $\hat{f}$, $\hat{g}$ of System 1 and f, g of System 3 under load change

(b) i_d and i_q waveforms of System 1 and System 3 under load change

(d) e_{v_m} and $l(t)$ of system 1 under load change

FIGURE 8 | Comparison of System 1 and System 3 under load change.

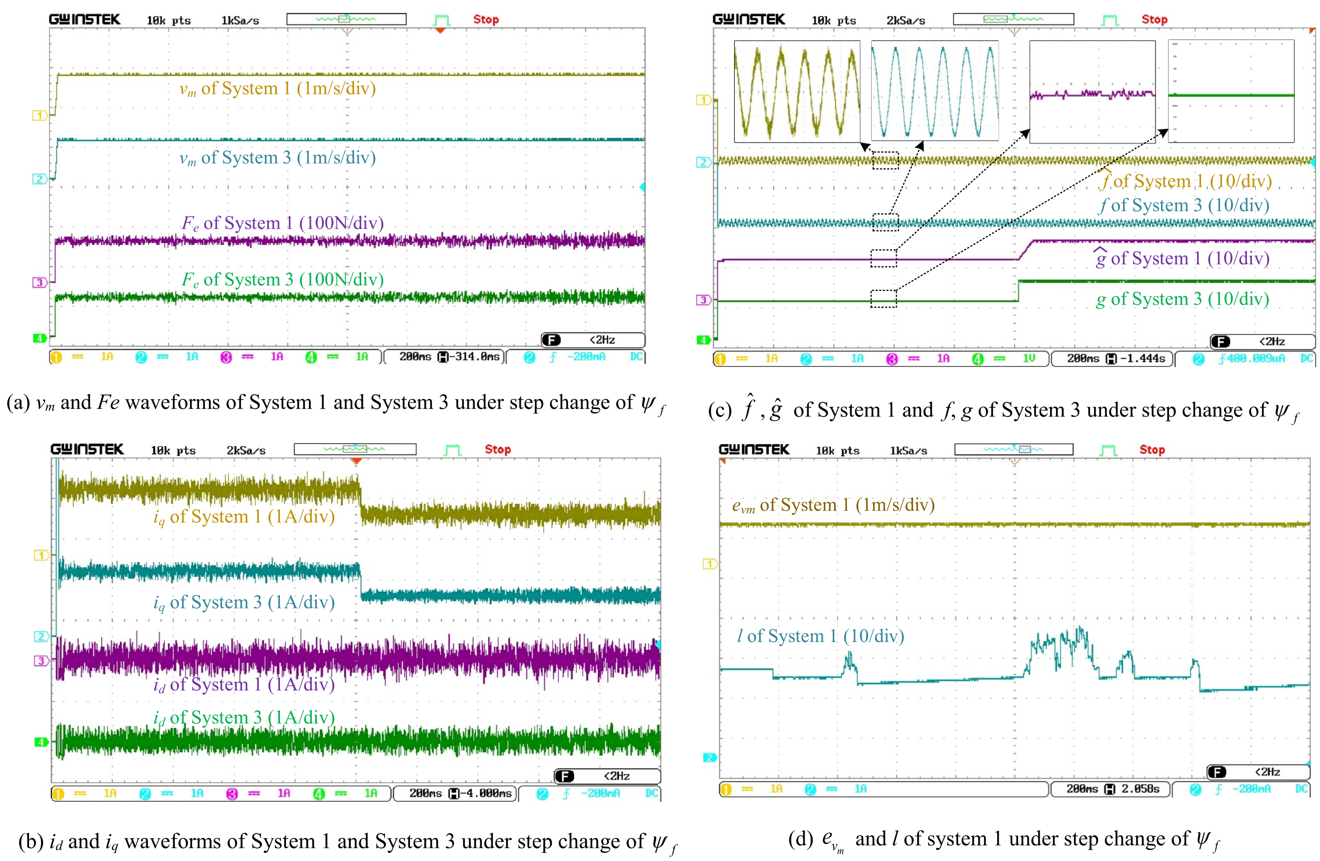

(a) v_m and Fe waveforms of System 1 and System 3 under step change of ψ_f

(c) $\hat{f}$, $\hat{g}$ of System 1 and f, g of System 3 under step change of ψ_f

(b) i_d and i_q waveforms of System 1 and System 3 under step change of ψ_f

(d) e_{v_m} and l of system 1 under step change of ψ_f

FIGURE 9 | Comparison of System 1 and System 3 under step change of ψ_f.

TABLE 3 | Specification comparison between System 1 and System 3.

Operation conditions	System	Ripple of v_m (m/s)	Overshoot of v_m (m/s)	Ripple of F_e (N)	Ripple of i_d (A)	Ripple of i_q (A)
v_{mref} change	System1	0.08	0	30	0.3	0.4
	System3	0.05	0	25	0.25	0.3
F_l change	System1	0.08	0	30	0.3	0.3
	System3	0.06	0	25	0.25	0.25
ψ_f change	System1	0.05	0	30	0.3 before ψ_f change	0.3 before ψ_f change
					0.3 after ψ_f change	0.3 after ψ_f change
	System3	0.04	0	25	0.2 before ψ_f change	0.2 before ψ_f change
					0.2 after ψ_f change	0.2 after ψ_f change

constructed. Next, an RBFNN estimator was put forward to estimate the unknown parameters of the ultralocal model, in which its weight matrices were adaptively updated online, and its centre values and widths were iterated by the K-means clustering method online. Finally, by combining MFAST and RBFNN estimator, the RBFNN-based MFAST control strategy was developed and its stability was meticulously analysed. StarSim HIL experiments verified that the proposed control strategy can significantly enhance robustness against various disturbances and improve dynamic performance, while attenuating system ripples. Without knowledge of any motor parameters, the proposed model-free strategy is especially fit for practical engineering. As a result, the MFAST control strategy-based RBFNN estimator offers a new intelligent method for PMLSM drive systems.

As the proposed MFAST control strategy is robust to the parameter and load uncertainties, it can be employed for the efficient system-level robust design optimization of electrical drive systems to improve the steady-state and dynamic performance [33, 34]. This will be considered in our future work. Moreover, different machine learning models will be investigated and compared for the model-free control of electrical machines.

Author Contributions

Qingfang Teng: conceptualization, formal analysis, funding acquisition, investigation, methodology, supervision, writing – original draft. **Xiaojian Wang:** formal analysis, investigation, methodology, software, writing – original draft. **Kai Xu:** writing – revision, validation.

Acknowledgements

This study has been supported by the National Natural Science Foundation of China (No. 61463025, No. 62063015). Open access publishing facilitated by University of Technology Sydney, as part of the Wiley - University of Technology Sydney agreement via the Council of Australian University Librarians.

Conflicts of Interest

The authors declare no conflicts of interest.

Data Availability Statement

The authors have nothing to report.

References

1. Y. Kung, "Design and Implementation of a High-Performance PMLSM Drives Using DSP Chip," *IEEE Transactions on Industrial Electronics* 55, no. 3 (2008): 1341–1351, https://doi.org/10.1109/tie.2007.909736.

2. Q. Tan, X. Huang, L. Li, and M. Wang, "Magnetic Field Analysis and Flux Barrier Design for Modular Permanent Magnet Linear Synchronous Motor," *IEEE Transactions on Industrial Electronics* 67, no. 5 (2019): 3891–3900, https://doi.org/10.1109/tie.2019.2918477.

3. T. Dong, R. Fu, B. Zhang, B. Peng, and X. Wei, "Analysis of Permanent Magnet Linear Synchronous Motor Made by Oriented Silicon Steel Sheet," *IEEE Transactions on Industry Applications* 59, no. 3 (2023): 3332–3340, https://doi.org/10.1109/tia.2023.3253816.

4. D. Fu, X. Zhao, and J. Zhu, "A Novel Robust Super-Twisting Nonsingular Terminal Sliding Mode Controller for Permanent Magnet Linear Synchronous Motors," *IEEE Transactions on Power Electronics* 37, no. 3 (2021): 2936–2945, https://doi.org/10.1109/tpel.2021.3119029.

5. K. Zhang, L. Wang, and X. Fang, "Adaptive Nonlinear Speed Tracking Control of Permanent Magnet Linear Synchronous Motor Based on I&I Theory," *IEEE Transactions on Industry Applications* (2024).

6. W. Xu, K. Liao, J. Ge, et al., "Improved Position Sensorless Control for PMLSM via an Active Disturbance Rejection Controller and an Adaptive Full-Order Observer," *IEEE Transactions on Industry Applications* 59, no. 2 (2022): 1742–1753, https://doi.org/10.1109/tia.2022.3230729.

7. Z. Li, J. Wang, J. An, et al., "Control Strategy of Biaxial Variable Gain Cross-Coupled Permanent Magnet Synchronous Linear Motor Based on MPC-MRAS," *IEEE Transactions on Industry Applications* 58, no. 4 (2022): 4733–4743, https://doi.org/10.1109/tia.2022.3170535.

8. S. Y. Chen, H. H. Chiang, T. S. Liu, and C. H. Chang, "Precision Motion Control of Permanent Magnet Linear Synchronous Motors Using Adaptive Fuzzy Fractional-Order Sliding-Mode Control," *IEEE* 24, no. 2 (2019): 741–752, https://doi.org/10.1109/tmech.2019.2892401.

9. M. Wang, K. Kang, C. Zhang, and L. Li, "Precise Position Control in Air-Bearing PMLSM System Using an Improved Anticipatory Fractional-Order Iterative Learning Control," *IEEE Transactions on Industrial Electronics* 71, no. 6 (2023): 6073–6083, https://doi.org/10.1109/tie.2023.3290251.

10. D. Fu and X. Zhao, "A Novel Robust Adaptive Nonsingular Fast Integral Terminal Sliding Mode Controller for Permanent Magnet Linear Synchronous Motors," *IEEE Journal of Emerging and Selected Topics in Power Electronics* 11, no. 2 (2022): 1672–1683, https://doi.org/10.1109/jestpe.2022.3229904.

11. L. Wang, J. Zhao, Z. Yu, Z. Pan, and Z. Zheng, "Robust and High-Precision Position Control of PMLSM-Driven Feed Servo System Based on Adaptive Fast Nonsingular Terminal Sliding Mode," *IEEE Transactions on Transportation Electrification* 11, no. 1 (2024): 4882–4894: Early Access Article, https://doi.org/10.1109/tte.2024.3471771.

12. S. Mondal and C. Mahanta, "Chattering Free Adaptive Multivariable Sliding Mode Controller for Systems With Matched and Mismatched Uncertainty," *ISA Transactions* 52, no. 3 (2013): 335–341, https://doi.org/10.1016/j.isatra.2012.12.007.

13. W. Qi, X. Yang, J. H. Park, J. Cao, and J. Cheng, "Fuzzy SMC for Quantized Nonlinear Stochastic Switching Systems With Semi-Markovian Process and Application," *IEEE Transactions on Cybernetics* 52, no. 9 (2021): 9316–9325, https://doi.org/10.1109/tcyb.2021.3069423.

14. M. Derbeli, O. Barambones, M. Farhat, J. A. Ramos-Hernanz, and L. Sbita, "Robust High Order Sliding Mode Control for Performance Improvement of PEM Fuel Cell Power Systems," *International Journal of Hydrogen Energy* 45, no. 53 (2020): 29222–29234, https://doi.org/10.1016/j.ijhydene.2020.07.172.

15. M. Zhou, H. Su, Y. Feng, K. Wei, W. Xu, and J. Cheng, "Super-Twisting Algorithm-Based Fractional-Order Sliding-Mode Control of Nonlinear Systems With Mismatched Uncertainties," *IEEE Transactions on Industrial Electronics* 71, no. 8 (2024): 9510–9519, https://doi.org/10.1109/tie.2023.3329164.

16. B. Kelkoul and A. Boumediene, "Stability Analysis and Study Between Classical Sliding Mode Control (SMC) and Super Twisting Algorithm (STA) for Doubly Fed Induction Generator (DFIG) Under Wind Turbine," *Energy* 214 (2021): 118871, https://doi.org/10.1016/j.energy.2020.118871.

17. M. Fliess and C. Join, "Model-Free Control and Intelligent PID Controllers: Towards a Possible Trivialization of Nonlinear Control," *IFAC Proceedings Volumes* 42, no. 10 (2009): 1531–1550, https://doi.org/10.3182/20090706-3-fr-2004.00256.

18. N. Yang, S. Zhang, X. Li, et al., "A New Model-Free Deadbeat Predictive Current Control for PMSM Using Parameter-Free Luenberger Disturbance Observer," *IEEE Journal of Emerging and Selected Topics in Power Electronics* 11, no. 1 (2022): 407–417, https://doi.org/10.1109/jestpe.2022.3192883.

19. K. Zhao, N. Jia, J. She, et al., "Robust Model-Free Super-Twisting Sliding-Mode Control Method Based on Extended Sliding-Mode Disturbance Observer for PMSM Drive System," *Control Engineering Practice* 139 (2023): 105657, https://doi.org/10.1016/j.conengprac.2023.105657.

20. S. A. Davari, S. Azadi, F. Flores-Bahamonde, F. Wang, P. Wheeler, and J. Rodriguez, "Compensating the Measurement Error in Model-Free Predictive Control of Induction Motor via Kalman Filter-Based Ultra-Local Model," *IEEE Transactions on Power Electronics* 39, no. 12 (2024): 15811–15821, https://doi.org/10.1109/tpel.2024.3443134.

21. Y. Zhang, J. Jin, and L. Huang, "Model-Free Predictive Current Control of PMSM Drives Based on Extended State Observer Using Ultralocal Model," *IEEE Transactions on Industrial Electronics* 68, no. 2 (2020): 993–1003, https://doi.org/10.1109/tie.2020.2970660.

22. H. Liu, W. Niu, and Y. Guo, "Direct Torque Control for PMSM Based on the RBFNN Surrogate Model of Electromagnetic Torque and Stator Flux Linkage," *Control Engineering Practice* 148 (2024): 105943, https://doi.org/10.1016/j.conengprac.2024.105943.

23. S. Shen and J. Xu, "Adaptive Neural Network-Based Active Disturbance Rejection Flight Control of an Unmanned Helicopter," *Aerospace Science and Technology* 119 (2021): 107062, https://doi.org/10.1016/j.ast.2021.107062.

24. V. Pesce, S. Silvestrini, and M. Lavagna, "Radial Basis Function Neural Network Aided Adaptive Extended Kalman Filter for Spacecraft Relative Navigation," *Aerospace Science and Technology* 96 (2020): 105527, https://doi.org/10.1016/j.ast.2019.105527.

25. H. Feng, Q. Song, S. Ma, et al., "A New Adaptive Sliding Mode Controller Based on the RBF Neural Network for an Electro-Hydraulic Servo System," *ISA Transactions* 129 (2022): 472–484, https://doi.org/10.1016/j.isatra.2021.12.044.

26. J. Kang, X. Huang, C. Xia, D. Huang, and F. Wang, "Ultralocal Model-Free Adaptive Super-Twisting Nonsingular Terminal Sliding Mode Control for Magnetic Levitation System," *IEEE Transactions on Industrial Electronics* 71, no. 5 (2023): 5187–5194, https://doi.org/10.1109/tie.2023.3285925.

27. X. Lin, R. Xu, W. Yao, et al., "Observer-Based Prescribed Performance Speed Control for PMSMs: A Data-Driven RBF Neural Network Approach," *IEEE Transactions on Industrial Informatics* 20, no. 5 (2024): 7502–7512, https://doi.org/10.1109/tii.2024.3357194.

28. N. Gu, D. Wang, Z. Peng, T. Li, and S. Tong, "Model-Free Containment Control of Underactuated Surface Vessels Under Switching Topologies Based on Guiding Vector Fields and Data-Driven Neural Predictors," *IEEE Transactions on Cybernetics* 52, no. 10 (2021): 10843–10854, https://doi.org/10.1109/tcyb.2021.3061588.

29. H. Yang and J. Liu, "An Adaptive RBF Neural Network Control Method for a Class of Nonlinear Systems," *IEEE/CAA Journal of Automatica Sinica* 5, no. 2 (2018): 457–462, https://doi.org/10.1109/jas.2017.7510820.

30. A. M. Ikotun, A. E. Ezugwu, L. Abualigah, B. Abuhaija, and J. Heming, "K-Means Clustering Algorithms: A Comprehensive Review, Variants Analysis, and Advances in the Era of Big Data," *Information Sciences* 622 (2023): 178–210, https://doi.org/10.1016/j.ins.2022.11.139.

31. J. A. Moreno and M. Osorio, "Strict Lyapunov Functions for the Super-Twisting Algorithm," *IEEE Transactions on Automatic Control* 57, no. 4 (2012): 1035–1040, https://doi.org/10.1109/tac.2012.2186179.

32. J. Liu, *Sliding Mode Control Design and MATLAB Simulation* (Tsinghua University Press, 2019).

33. G. Lei, Y. Guo, J. Zhu, T. S. Wang, X. M. Chen, and K. R. Shao, "System Level Six Sigma Robust Optimization of a Drive System With PM Transverse Flux Machine," *IEEE Transactions on Magnetics* 48, no. 2 (2012): 923–926, https://doi.org/10.1109/tmag.2011.2173795.

34. G. Lei, T. Wang, J. Zhu, Y. Guo, and S. Wang, "System-Level Design Optimization Method for Electrical Drive Systems—Robust Approach," *IEEE Transactions on Industrial Electronics* 62, no. 8 (2015): 4702–4713, https://doi.org/10.1109/tie.2015.2404305.